

Tensegrity Rings for Deployable Space Antennas: Concept, Design, Analysis, and Prototype Testing

Pier Luigi Ganga, Andrea Micheletti, Paolo Podio-Guidugli,
Lucio Scolamiero, Gunnar Tibert, and Valfredo Zolesi

Abstract In this paper we describe a tensegrity ring of innovative conception for deployable space antennas. Large deployable space structures are mission-critical technologies for which deployment failure cannot be an option. The difficulty to fully reproduce and test on ground the deployment of large systems dictates the need for extremely reliable architectural concepts. In 2010, ESA promoted a study focused on the pre-development of breakthrough architectural concepts offering superior reliability. This study, which was performed as an initiative of ESA Small Medium Enterprises Office by Kayser Italia at its premises in Livorno (Italy), with Università di Roma TorVergata (Rome, Italy) as sub-contractor and consultancy from KTH (Stockholm, Sweden), led to the identification of an innovative large deployable structure of tensegrity type, which achieves the required reliability because of a drastic reduction in the number of articulated joints in comparison with non-tensegrity architectures. The identified target application was in the field of large space antenna reflectors. The project focused on the overall architecture of a deployable system and the related design implications. With a view toward

P.L. Ganga (✉) • V. Zolesi
Kayser Italia srl, Livorno, Italy
e-mail: p.ganga@kayser.it; v.zolesi@kayser.it

A. Micheletti
Dipartimento di Ingegneria Civile e Ingegneria Informatica, University of Rome “Tor Vergata”,
Rome, Italy
e-mail: micheletti@ing.uniroma2.it

P. Podio-Guidugli
Accademia Nazionale dei Lincei, Rome, Italy

Department of Mathematics, University of Rome “Tor Vergata”, Rome, Italy
e-mail: ppg@uniroma2.it

L. Scolamiero
European Space Agency, ESA ESTEC, Noordwijk, The Netherlands
e-mail: Lucio.Scolamiero@esa.int

G. Tibert
Department of Aeronautical and Vehicle Engineering, KTH, Stockholm, Sweden
e-mail: tibert@kth.se

verifying experimentally the performance of the deployable structure, a reduced-scale breadboard model was designed and manufactured. A gravity off-loading system was designed and implemented, so as to check deployment functionality in a 1-g environment. Finally, a test campaign was conducted, to validate the main design assumptions as well as to ensure the concept's suitability for the selected target application. The test activities demonstrated satisfactory stiffness, deployment repeatability, and geometric precision in the fully deployed configuration. The test data were also used to validate a finite element model, which predicts a good static and dynamic behavior of the full-scale deployable structure.

List of Symbols

- n Number of bars in the tensegrity prism (TP)
- a Lower TP radius
- b Upper TP radius
- h TP height
- φ TP twist angle (for short, the twist)
- h^* "Overlap" between two successive stages of a symmetric Snelson tower/Snelson ring
- γ a/b ratio between the TP radii
- δ h^*/h ratio between TP height and Snelson tower/Snelson ring overlap
- H_s Stowed height of the deployable tensegrity ring

1 Introduction

Large deployable space antenna reflectors (LDRs), with diameters between 4 and 25 m, are required in several mission types, particularly in the telecommunication domain, but also for Earth observation, deep-space missions, and radio-astronomy [9].

To be deployed once in orbit, reflectors with diameter in excess of 4–5 m must have a foldable structure for compatibility with the launcher's available storage. When associated with the need for extreme deployment reliability, the demanding mechanical, thermal, and radio-frequency requirements of the as-deployed reflector result in very challenging, multidisciplinary design issues. As a consequence, very few companies specialize in the production of such large reflectors, most of them being based in the USA (Northrop-Grumman, Harris Corporation) and subject to US exporting regulations.

Due to the emerging market of small and microsattellites and the stringent storage requirements dictated by small launcher fairings, the foldability requirement may be imposed also to much smaller reflectors (down to 2 m in diameter); therefore, LDR technology is a potential candidate for much larger a class of antenna reflectors.

With a view toward reducing dependence on non-EU suppliers, ESA is pursuing developments in this domain. In particular, within the frame of an initiative of the ESA Small Medium Enterprises Office (<http://www.esa.int/SME/>), the study of a potentially breakthrough technology has been undertaken, whose goal was to conceive a deployable large antenna reflector of intrinsically high reliability. A concept validation by testing a reduced-scale breadboard model has been performed.

This paper reports the outcome of the above mentioned activities, namely the conception of an innovative large deployable structure based on “tensegrity” principles, currently being protected by an international patent filing [17].

2 Large Space Deployable Reflectors

The need for LDRs of 4–25 m in diameter is well established [9]; in fact, the market goes beyond pure telecommunication missions (still the major users of such technology), and spans from Earth observation, navigation, and deep-space missions, to radio-astronomy.

Operative radio-frequency bands go from the lowest P-band frequencies up to L-S, Ku and higher, and finish with Ka, the band reserved for small-diameter reflectors, typically about 5 m in diameter. Several 12-m reflectors have already successfully flown, and recent missions have embarked and successfully deployed reflectors up to 18 and 22 m in diameter.

To comply with the demanding radio-frequency needs, as-deployed shape accuracy and high stability in operational conditions (for the entire operational life) are required. To limit the overall reflector mass, high-stability/low-density materials and technologies are utilized, with large use of carbon fiber reinforced plastics (CFRP) for rigid structural members. Subtler radio-frequency phenomena (known as passive inter modulation products—PIMP) pose even stricter requirements on candidate materials, processes, and thermo-mechanical design solutions.

2.1 LDR Classification and State of the Art

Here follows a brief overview and classification of the state-of-the-art LDR architectures and the relative mission applications [9].

2.1.1 Mesh Reflectors

This is by far the most successful technology, based on a tension-truss concept and metal tricote mesh as reflective layer. The mesh is knitted with gold plated tungsten or molybdenum wires (15–25 μm diameter), and it needs to be subjected to a tension between 5 and 10 g/cm both to achieve adequate electrical contact between wires and to prevent PIMP problems. To provide the required mesh tension and shape accuracy simultaneously is a challenging task, due to the detrimental phenomenon known as “pillow effect” (or “facet effects”) which occurs when controlling the mesh surface in a limited number of points. Among mesh reflectors, two different mechanical and deployment architectures dominate the market: the *peripheral expandable ring* and the *hinged radial ribs* architectures.

In the former architecture, the peripheral expandable ring applies tension to two paraboloidal triangular networks. The two tensile networks provide shape and pre-tension to the underlying radio-frequency reflective mesh layer (this is the case, e.g., for the AstroMesh reflector by AstroAerospace, now Northrop Grumman, Fig. 1, [20]). LDRs belonging to this category have been supplied by Northrop Grumman and flown on the following telecommunication missions: Inmarsat-4, Alphasat (Inmarsat-XL), Thuraya-1,-2,-3, MBSAT, and SMAP for an Earth Observation mission.

Hinged radial ribs reflectors are based on multiple, rigid, radial compressive elements to apply tension to the radio-frequency reflective mesh. Cable nets and cable ties provide the mesh with the required shape (Fig. 2). Harris has supplied reflectors based on this architectures for the following telecommunications missions: SkyTerra-1, TerreStar-1 (now EchoStar-1) ICO-G1, MexSat-1, and MexSat-2.



Fig. 1 Astro-Mesh 14 by 11 m peripheral expandable ring concept (image by Northrop Grumman via spacenews.com/northrop-unit-delivers-alphasat-1-xl-reflector/)



Fig. 2 TerreStar 18 m diameter reflector (image by Harris Corporation, harris.com/harris/whats_new/TerreStar-reflector.jpg)

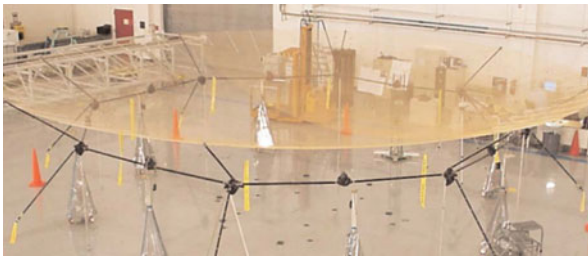


Fig. 3 Hoop-truss reflector (image by Harris Corporation via www.propagation.gatech.edu/ECE6390/project/Fall2010/Projects/group4/comm.html)

Variations to these two basic architectures do exist, e.g., the “Hoop-Truss reflector,” also called “Double pantograph ring” or “Conical pantograph ring,” in Fig. 3 (ESA patents: 568–596, US patent US 9153860 B2) but there are no known flight applications to date.

Europe is very active in the domain of metallic mesh based LRDs, and aims to achieve technological independence from non-European suppliers in this strategic domain. Among other activities, ESA is performing technology research and development activities in the domain of basic metallic-mesh materials [16] and in the domain of alternative deployment architectures, focusing on dimensional scalability and modularity of the concepts, so as to cover diameters from 5 to 18 m and more while maintaining cost effectiveness of the final product [16]. Many reduced-scale (typically, 4 m in diameter) ground demonstrators have been produced.

It is worth noticing that very recently ESA has selected the 12 m LDR for the 7th Earth Explorer mission: BIOMASS, set for launch in 2020 [3]. The selected deployable reflector technology falls in the domain of hinged radial rib reflectors, supplied by Harris Corporation.

2.1.2 Membrane and Inflatable Reflectors

These reflectors consist of a thin membrane of metallized polyimide films. They need first to be inflated, in order to achieve the required shape and surface accuracy, then to be made rigid (via thermal or UV curing of associated resin systems) to maintain shape and stiffness during their operational life. Notably, the ESA 12 m diameter inflatable rigidizable reflector (Fig. 4), and the JPL L.Garde 14 m inflatable antenna demonstrator, were flown in 1996 on board the STS-77 mission (Fig. 5). The major limit of this technology is the modest achievable surface accuracy, the



Fig. 4 ESA—Contraves—RUAG (CH) inflatable space rigidized structure (image by Contraves via www.thespaceoption.com/cres_mcbc.php)



Fig. 5 Inflatable antenna experiment—NASA JPL—L. Garde (image by L.Garde, www.lgarde.com/deployable-antennas.php)

reason why reflectors of this kind are still at the level of prototypes and technology demonstrators, and can only be utilized at lower range of radio-frequency bands.

2.1.3 Shell-Membrane Reflectors

These reflectors are based on a triaxially woven carbon-fiber fabric, reinforcing a space-qualified silicon matrix (CFRS). Developed by the Technical University of Munich—LLB, this material allows for full foldability of the reflecting surface, preserving the high dimensional stability and radio-frequency properties of the carbon-fiber layers. The main advantage with respect to classical metallic-mesh reflectors is that there is no need of tensioning a mesh, and hence no “pillow effect.” Developments are on-going in Europe [2], although there has been no flight mission application to date.

2.1.4 Largely Deformable Shell Reflectors

These reflectors provide a very elegant and mass efficient solution. They are very popular although currently limited in diameter size (no more than 6–8 m). This class of reflectors is well represented by the “Spring Back Antenna” from Hughes Space and Communication Group, now Boeing Satellite Systems Inc., for data relay satellite missions (Fig. 6).

Fig. 6 Boeing Satellite System (former Hughes Space and Communication) Spring Back Antenna reflector (image by Boeing Satellite Systems via www.nasa.gov/topics/technology/features/tdrs-upgrade.html)



Fig. 7 Boeing Satellite System (former Hughes Space and Communication) foldable rigid panels reflector (image by Boeing Satellite System via www.spacedaily.com/news/xm-radio-01c.html)



2.1.5 Solid Surface Reflectors

The best example of this architecture is the XM Satellite Radio antenna reflectors from Hughes Space and Communication International (Fig. 7), now Boeing Satellite System Inc. Also in this case, diameters do not exceed 6–8 m; their surface accuracy is better than that of deformable shell reflectors, and they also allow for “surface shaping” features (*ad hoc* deviations from a nominal paraboloid) improving radio-frequency performances.

2.2 LDR State-of-the-Art Assessment

What makes antenna reflectors unique in terms of design challenges is the need for extreme deployment reliability: a deployment failure would most of the times result in mission loss, an unacceptable option.

Several concepts have been studied worldwide to combine the reflector-specific set of multidisciplinary requirements and the fundamental need of an absolutely reliable deployment. However, the very specialized competencies required, and the amount of investment necessary to develop/qualify reliable products, have resulted in very few companies offering commercially qualified units, the most prominent being Harris Corporation [5] and Northrop-Grumman [13].

The experience gained by the major large reflector suppliers notwithstanding, the deployment of such items is always a critical step in a mission scenario. Indeed, the typical structure to be deployed consists of a large number of interconnected rigid elements. As a consequence, a large number of mechanical joints (either simply revoluted or telescopic, or motorized, joints) are necessary to fold the structure when in launch configuration and to deploy it in orbit.

Mechanical joints/hinges, and “mechanisms” in general, are typically sources of reliability concern, in that they may induce localized failures. The starting point of the development presented in this paper is that a system with a minimal number of joints would have optimal reliability, because of the low number of single-point failure sources.

The possibility of using a structural architecture of “tensegrity” type, where mechanical joints are in principle totally absent from the design, was then considered. The idea of using “tensegrity”-type structures for large antenna applications is not new, and in fact it has been the subject of a related patent [19]. However, it is our opinion that the new ideas we conceived in the course of our study, and the new design features we introduced, make the final design original and unique, so much so as to deserve an international patent filing [17].

In the following sections, we shall describe the technical features of the structural architecture we propose, as well as its validation by means of the realization of a scaled model breadboard and a test campaign.

3 Tensegrity Structure Description

3.1 Definition

Tensegrity structures (TS) were first conceived by the artist Kenneth Snelson [4, 18] in 1948. In the 1960s, Snelson began to build a number of outdoor sculptures, which made tensegrities worldwide popular among architects and engineers because of their innovative structural concept. Indeed, when an architect or a structural engineer looks at a realization of Snelson’s, he observes that:

- TSs are pre-stressed spatial frameworks whose elements are bars and cables;
- cables form a connected set, i.e., tens(ile int)egrity;
- bar ends never touch (floating compression).

In addition, TSs possess the important *form-finding property*, to be described in Sect. 3.3.

3.2 The Tensegrity Prism

A regular n -bar tensegrity prism (TP) is a cyclic-symmetric structure with an n -fold axis of cyclic-symmetry, always taken vertical. As shown in Fig. 8, a TP can have

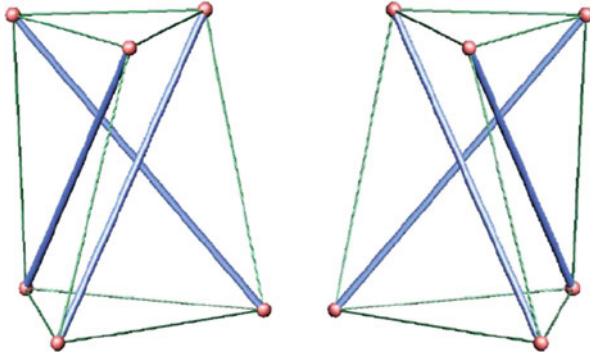
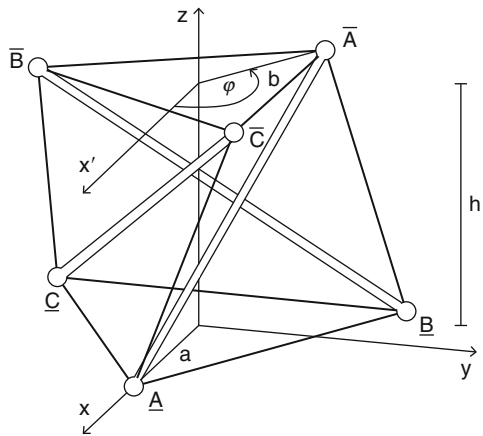


Fig. 8 The simplest three-dimensional TS: two tensegrity prisms with opposite chirality

Fig. 9 The TP parameters



two different orientations. The geometry of a TP can be identified by means of five parameters (Fig. 9):

- the number of bars n ,
- the lower “radius” a ,
- the upper “radius” b ,
- the height h ,
- the twist angle φ (for short, the *twist*).

3.3 Form-Finding Property

As observed by Oppenheim and Williams [14], form-finding (FF) is a property that becomes evident when we try to build a TS by hand. Let us suppose that we have what is necessary to assemble one of the systems in Fig. 8, all elements having a fixed length. Once all but one connections between elements are realized, we notice that the so obtained partial assembly has no stiffness, and that there are many possible configurations with slack cables. If the last element is a cable (a bar), its length is determined when we try to decrease (increase) the distance between the two nodes to be connected. As soon as that distance reaches a minimum (maximum) value, the system takes its shape. If we force the two nodes to get closer (farther), then the system acquires a self-stress state with the last element in tension (compression). Figure 10 illustrates the FF property in the simplest case. With this example in mind, we can state the FF property as follows: “Given an N -elements tensegrity system, if the lengths of $(N - 1)$ elements are fixed, then a stable equilibrium configuration is obtained when the last cable (bar) has minimal (maximal) length.”

For a fixed topology, i.e., once a collection of nodes connected by bars and cables is chosen, it is possible to pass from one stable configuration to another simply by changing the lengths of two or more elements.

Due to the FF property, a tensegrity system is stable only for a restricted set of configurations. For example, in the system in Fig. 10, stable configurations are those with the three nodes collinear. The problem of finding the set of stable configurations for a given tensegrity system, referred to as the *form-finding problem*, has been extensively studied in the literature [6, 21].

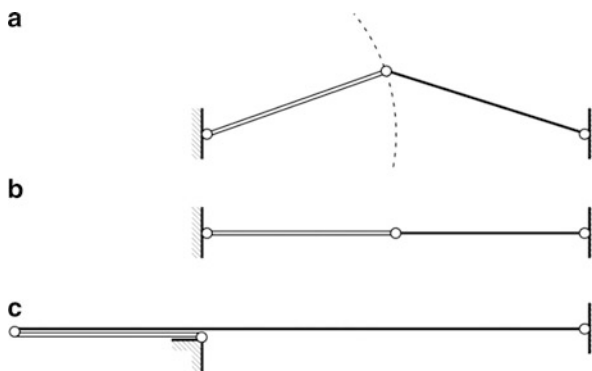


Fig. 10 The form-finding property for a system composed of two elements. The double-line element has fixed length; the single-line element has variable length. The central node can only be on the dashed circumference shown in (a). On progressively shortening (lengthening) the single-line element, configuration (b), (c) is reached; on further shortening (lengthening) the same element, the system is found in a self-stress state with that element in tension (compression)

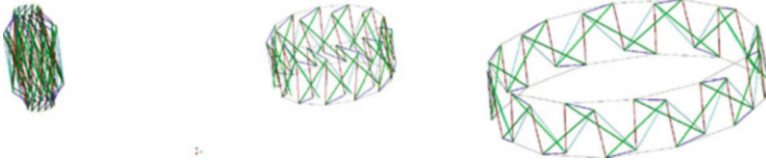


Fig. 11 TS theoretical ring in different equilibrium configurations

3.4 *Tensegrity Deployable Structures*

The FF property of tensegrity systems and their related capability to change shape suggest to have recourse to such systems when it is desirable to have deployable or variable-geometry structures, or “smart” structures, some elements of which serve as sensors and actuators. By actuating cables and/or bars, a TS can pass from one equilibrium configuration to another through a continuous path of equilibrium configurations (Fig. 11 shows a TS ring in different equilibrium configurations). Due to the absence of hinges between bars, the mechanical behavior of a floating-compression system can be predicted with better accuracy than for conventional hinged systems.

3.5 *Tensegrity Rings for Space Structures*

The first studies of ring-shaped TS’s appear to be performed by Burkhardt [1] in 2003; a tensegrity torus was analyzed by Peng et al. in 2006 [15] and by Yuan et al. in 2008 [22]. The deployable tensegrity ring that we here consider has been presented for the first time in [23]. The same kind of tensegrity ring has been studied in [7].

The tensegrity ring (TR) concept is suitable for disc- or ring-shaped space structures. Since bars are not connected to each other, none of the usual hinge mechanisms are present in TS’s: freedom in spatial orientation and relative motion of bars during deployment is granted by the flexibility of the interconnecting cables. The absence of mechanical joints reduces the possible failure modes of the deployable system, thus increasing its overall reliability, a fundamental requirement for this type of space technology; in addition, this feature permits an especially tight and compact stowage of the structure. Finally, as is the case with conventional pin-jointed trusses, none of the individual members is bent, sheared, or twisted.

We named the tensegrity ring we developed for the present application “Snelson ring” (SR). SR is a TR with the same graph as a two-level Snelson tower. To obtain a Snelson tower, we “superimpose” a number of tensegrity prisms (TP) (as shown in Fig. 12) by repeating the following sequence of steps:

1. we take two prisms with opposite orientations;
2. we remove the lower cables of the upper prism;

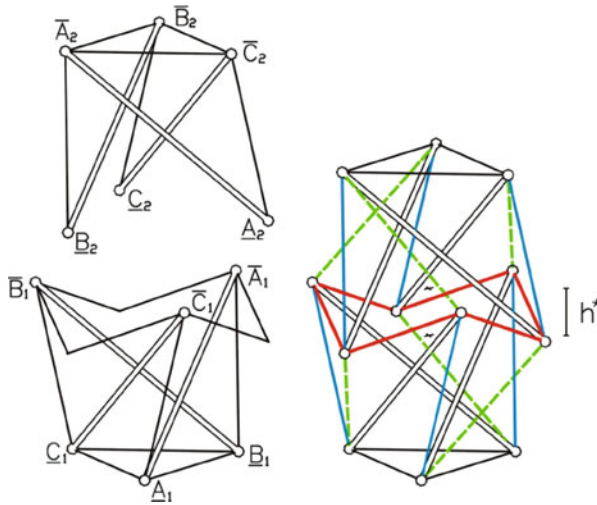


Fig. 12 Superposition of two TPs to obtain a two-level Snelson tower

3. we connect the lower nodes of the upper prism with the middle points of the upper base cables of the lower prism;
4. we add $2n$ additional cables (in green in Fig. 12).

In an SR, we distinguish four groups of cables according to position, in such a way that symmetrically placed cables belong to the same group. The cables in these groups are named as follows:

- “verticals,” when they connect bars of the same TP;
- “diagonals,” when they connect bars of different TPs;
- “saddles,” when they belong to both TPs;
- “polygons,” when they form base polygons.

In Fig. 12, verticals, diagonals, and saddles are depicted, respectively, in blue, green, and red.

The geometry of symmetric Snelson towers can be identified by six parameters, namely the above-defined five parameters (n, a, b, h, φ) of a typical TP plus a new parameter:

h^* is the “overlap“ between stages (see Fig. 12).

Note h^* is null when saddles lay on the same horizontal plane. Three additional geometric properties are used to characterize a deployable SR:

δ is the overlap ratio (h^*/h) between the Snelson tower/Snelson ring overlap and the TP height;

γ is the ratio (a/b) between the two radii of a typical TP;

H_s is the stowed height of the deployable tensegrity ring.

The form-finding condition for TP and SR has been obtained in the literature by different authors; here we make use of the conditions given in [10]. For TPs, the form-finding condition:

$$\varphi = \frac{\pi}{n} + \frac{\pi}{2} = \varphi_0$$

involves only n and φ . For $\theta := \varphi - \varphi_0$, the form-finding condition for SRs:

$$\begin{aligned} \delta^2(\gamma \sin \varphi_0 + \sin \theta) + \delta(\gamma - \gamma \sin \varphi_0 + 2 \sin \varphi_0 \sin \theta - 2 \sin \theta) + \\ -2 \sin \varphi_0 \sin \theta + 2 \sin \theta = 0 \end{aligned} \quad (1)$$

involves the full set of parameters, namely n , φ , γ , and δ . In Fig. 13, δ is plotted versus φ for various values of γ and for $n = 6$ and $n = 12$. We see that ring-shaped Snelson towers obtain for small twists and large overlaps.

3.6 Deployment Strategy

A TR can be deployed by changing the length of some of its elements so as to obtain the desired change in shape from stowed to deployed configurations. For the SR considered for the present application, it was chosen to change the length of a subset of cables, while keeping constant the lengths of the remaining cables and of all the bars. In order to have a slow, smooth, and controllable deployment process, all the cables in the TR have to be kept in tension.

SRs have good properties with regard to their use as deployable structures. We found that SR can easily be deployed by lengthening the polygonal cables while shortening the vertical cables, as shown in Fig. 14. SRs have the important property of being *super-stable* [11], a feature that other types of TR lack. Super-stability implies that a structure is stable independently of the self-stress level and of its elastic properties, so that finding admissible deployment paths is simpler. It is worth noticing that super-stability of SRs does not depend on n .

The adopted deployment strategy consists of two phases:

- change in configuration, from folded to deployed (Deployment Phase 1);
- final pre-stressing, to reach a prescribed stress level in the system (Deployment Phase 2).

In the present study, Deployment Phase 1 has been simulated numerically by means of the procedure detailed in [12]; a custom-made finite element code has been used for the simulation of Deployment Phase 2. The feasibility of both phases has been verified in advance with the aid of small-scale models.

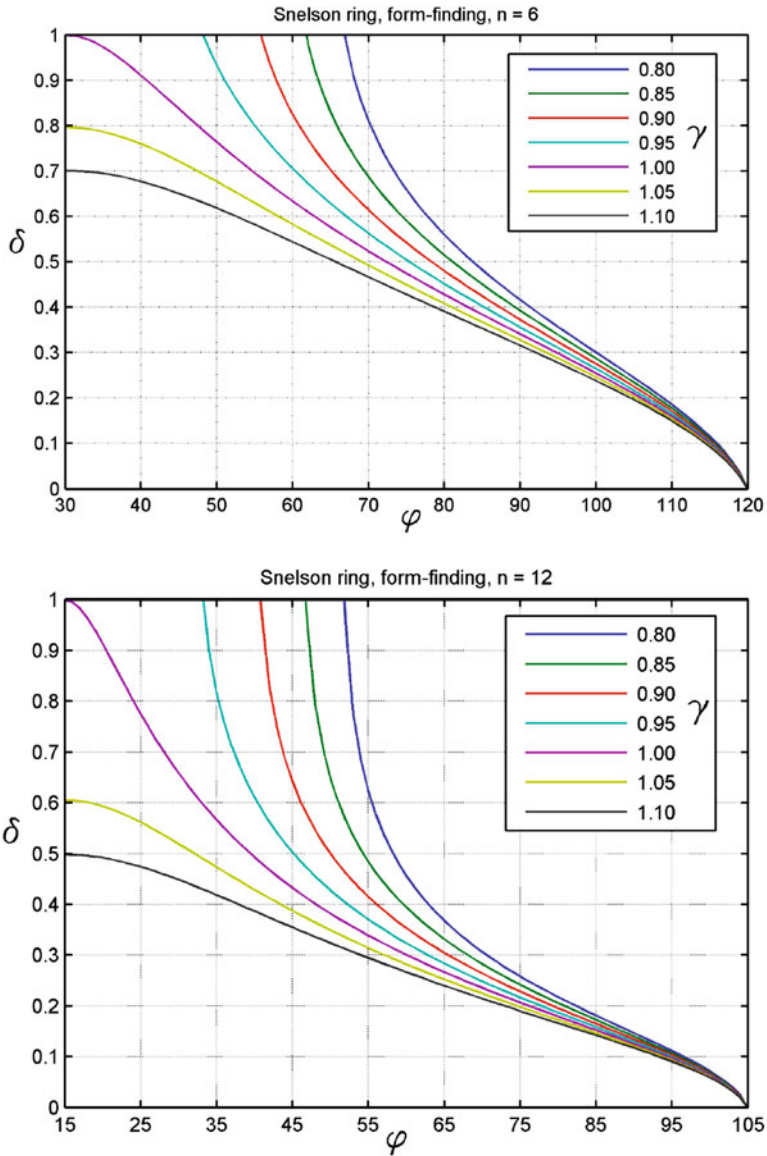


Fig. 13 Relation between δ and φ ($^\circ$) for various values of γ , $n = 6, 12$

3.6.1 Deployment Phase 1

During Deployment Phase 1, the change of configuration is obtained by changing only the lengths of two groups of cables: the polygonal cables lengthen, the vertical cables shorten. Figure 14 shows the stowed and the deployed configuration of a

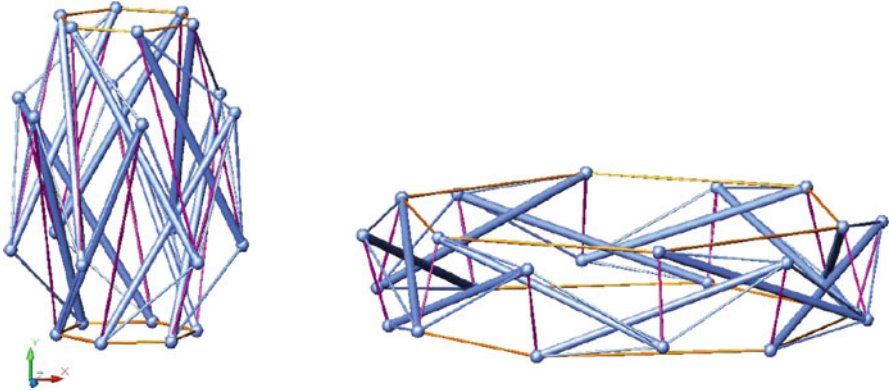


Fig. 14 A hexagonal TR, folded and deployed

hexagonal TR, one obtained from the other in this way (purple cables are shortened during deployment; orange cables are lengthened).

3.6.2 Deployment Phase 2

Due to the FF property, the pre-stress can be induced in the structure by acting on few cables only. These cables can be conveniently chosen among those not involved in Deployment Phase 1, on keeping in mind that the corresponding actuators are due to apply a large force to obtain a small change in length.

4 Tensegrity Space Structure Design

A deployable tensegrity ring of Snelson type (SR) was identified as the main structure in a tensegrity space structure (TSS) to be designed consistent with the following specifications, among others:

- Function: Deployable Antenna Reflector
- Operating frequency: from 6 to 14 GHz
- Reflective Mesh tension: 5 N/m
- Reflector diameter: 12 m
- Stowed height: about 4.4 m
- Stowed diameter: about 2.4 m (excluding the reflector-to-boom interface)
- Mass budget: 57 kg or less (excluding the spacecraft boom)
- Eigenfrequency (deployed, not including boom): 1.2 Hz (min), 1.5 Hz (target).

These specifications are compliant with the typical launcher's mechanical interface (i.e., stowed dimensions) and the typical deployed-to-folded diameter ratio.

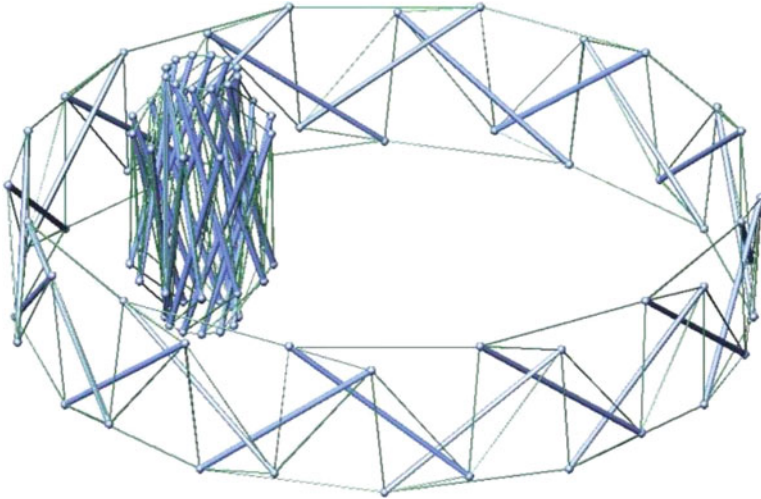


Fig. 15 TSS deployable tensegrity ring model

4.1 Tensegrity Ring Analysis

We considered a reflector of 12 m in diameter and 2.6 m in height, so as to accommodate the two paraboloids with a gap for the central tension-tie ($2.6 = 2 \times 1.25 + 0.1$). A parametric analysis of the SR was performed in the absence of the inner tension truss (also called web in the present document) (Fig. 15).

The FF analysis presented in Sect. 3.5 showed that suitable configurations have a small twist φ and a large overlap ratio δ . Note that it is not possible to have $\delta \geq 1$, since this would require that some cables take a compressive or null stress; moreover, having $\gamma > 1$ causes problems with regard to the clearance between bars. Given these constraints, we focused on those configurations having δ near but not greater than 1. Figure 16 shows a closer view of the form-finding solutions for $\gamma = 0.96, 0.98, 1.00$, and $n = 12$.

To pick a convenient set of geometric parameters, we looked at deployability; in particular, we computed an approximate value for the stowed height H_s , as the sum of the lengths of one bar and one diagonal cable. We did this because in the stowed configuration these elements, which are kept almost parallel to the vertical axis, span the height of the SR. The computed values are plotted in Fig. 17 for the same values of γ and n as before. These plots show that only for $\gamma = 1$ the stowed height requirement can be fulfilled. However, a precise computation with the procedure given in [12] gives smaller values of H_s , and by taking $\gamma = 0.98$ the resulting stowed height is $H_s = 4.53$ m.

Next, we looked at the clearance between bars, D_b , computed as the distance between their axes. Figure 18 shows that the clearance becomes very small as φ

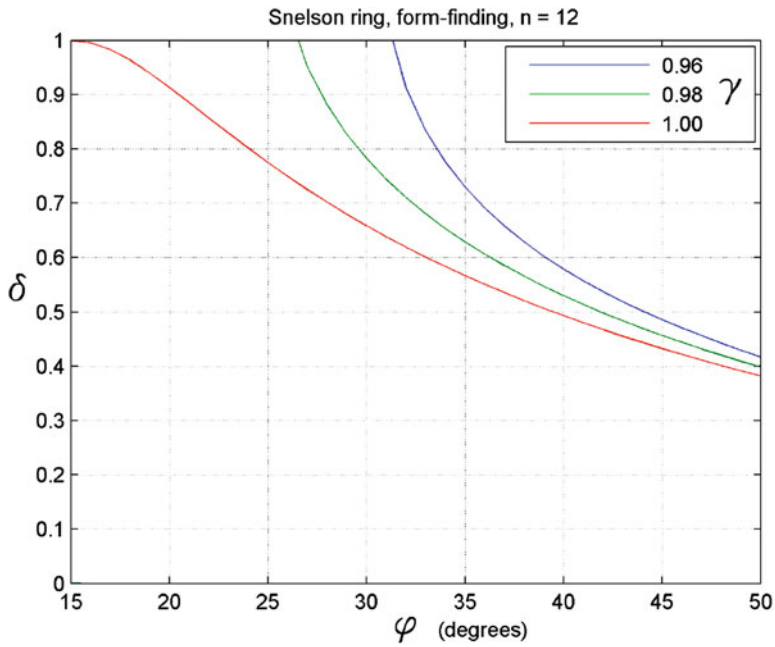


Fig. 16 A closer view of the form-finding solutions for an SR, $n = 12$

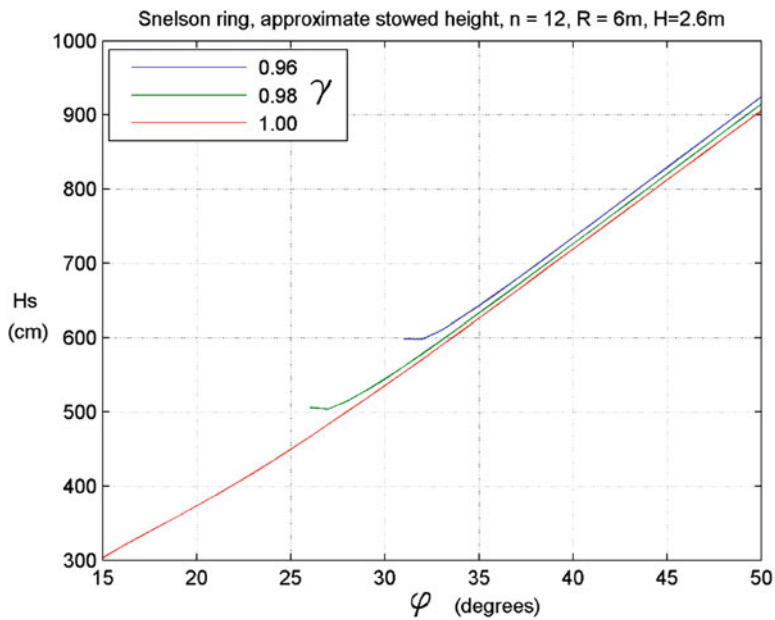


Fig. 17 Approximate stowed height versus φ for various values of γ , $n = 12$

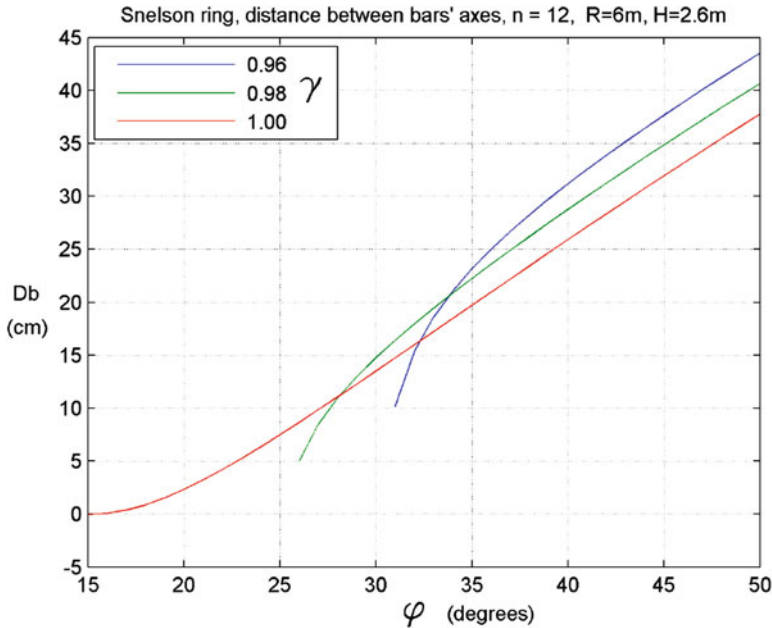


Fig. 18 Clearance between bars, $n = 12$

gets closer to the range of interest. Note that the behavior of both D_b and H_s does not change much when increasing n . Lastly, with a view toward dimensioning bars and cables, we checked bar lengths (Fig. 19) and stresses (Fig. 20).

All in all, the parameters chosen in order to provide a compact stowage of the ring, while maintaining good structural performances, are the following:

$$\varphi = 28^\circ, \quad \gamma = 0.98,$$

with, we recall, $n = 12$, a deployed diameter of 12 m, a deployed height of 2.6 m, and a stowed height of 4.53 m. Figure 15 shows such an SR, both folded and deployed. Figure 21 shows the height versus the base radius of the reflector during deployment. The plot of the clearance between bars versus the base radius during deployment in Fig. 22 shows that the clearance decreases monotonically and reaches a minimum value of about 0.11 m in the deployed configuration.

Remark. To match a web with six-fold symmetry, parameter n should be a multiple of 6. We found that, with $n = 6$, a 12 m reflector based on an SR cannot satisfy the stowage-height requirement, because bars would be excessively long; however, reflectors of smaller radius can have $n = 6$ and be conveniently designed in the same way described above. On the other hand, an SR with $n = 18$ would be too complex a structure for a 12 m reflector, requiring a larger number of actuators than an SR with $n = 12$; in addition, such an SR would also be a more, and possibly too much, flexible structure.

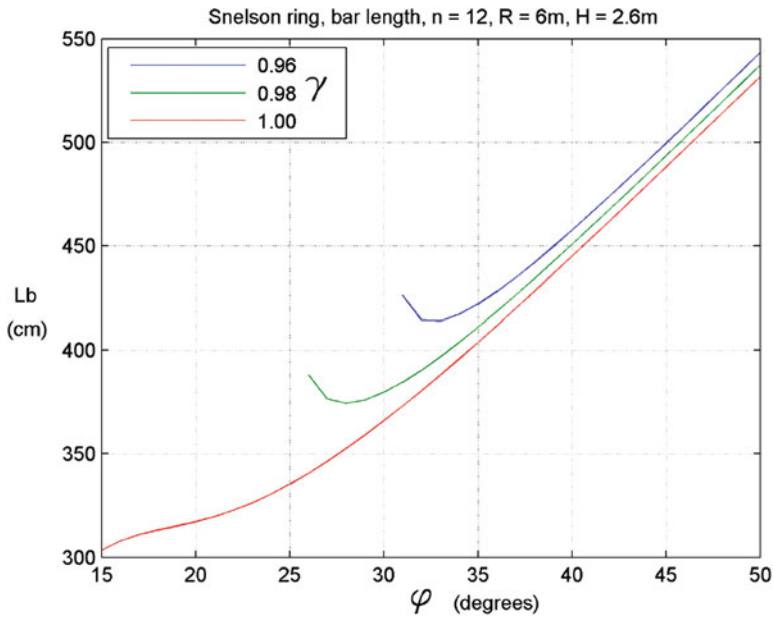


Fig. 19 Bar length, $n = 12$

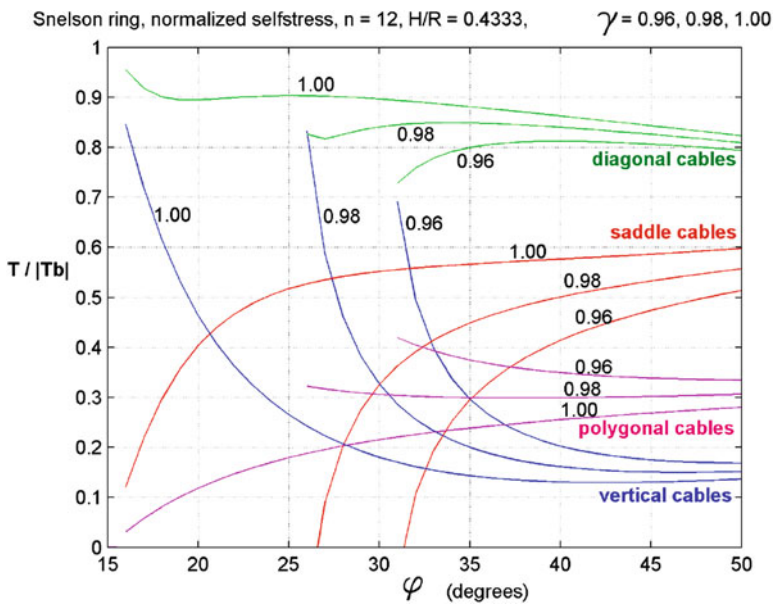


Fig. 20 Axial forces in cables, normalized with respect to the compressive force in bars

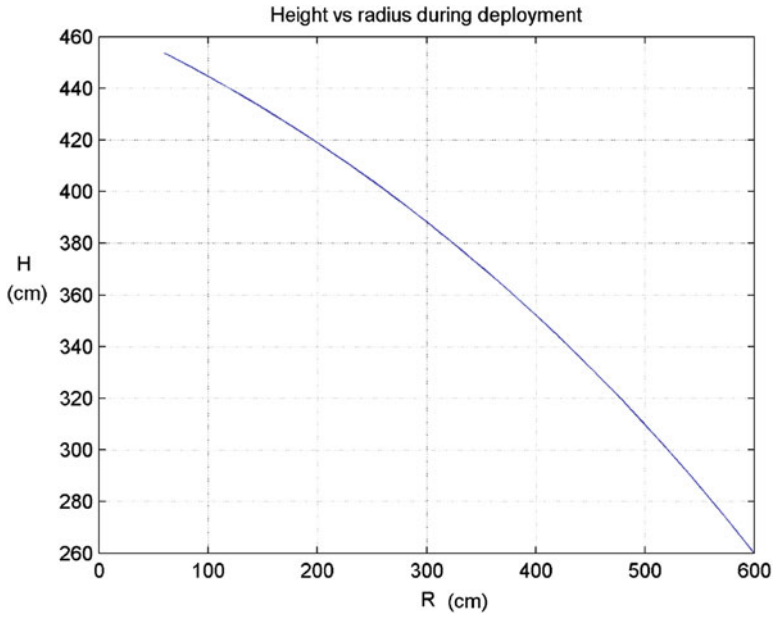


Fig. 21 Design of the reflector: height versus radius during deployment

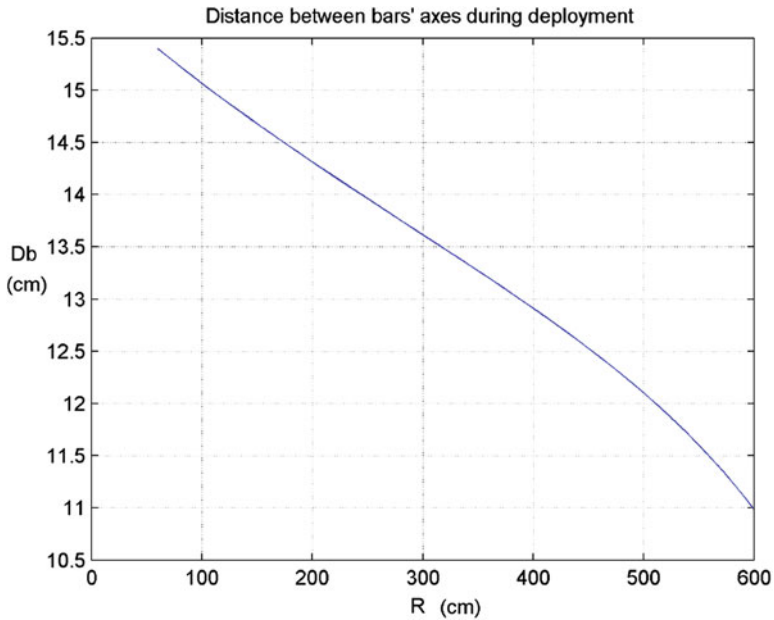


Fig. 22 Design of the reflector: clearance between bars during deployment

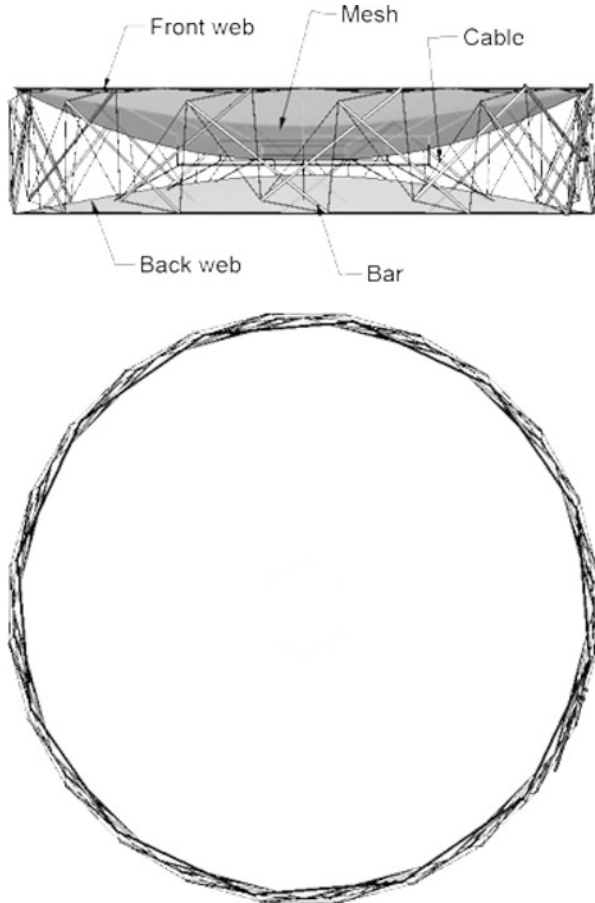


Fig. 23 TSS Flight Model deployed (TSS-to-Boom I/F not shown in the picture)

4.2 Flight Model Design

A preliminary design of the Flight Model (FM) of the TSS was performed, with the aim of investigating the expected physical and structural properties of the TSS when materials easily available on the market are used. The Flight Model is composed of the following elements: cables, bars, front and back web (in light gray in Fig. 23), reflective mesh (in heavy gray), deployment actuation system, tensioning actuation system, and TSS-to-Boom (spacecraft) apparatus I/F. The Flight Model is 12 m in diameter and 2.6 m in height in its deployed configuration, 2.33 m in diameter and 4.53 m in height when folded. All the 24 TSS TR bars are of the same fixed length. The overall calculated mass is 58 kg, including all the above mentioned elements and an additional 10% margin to take into account unavoidable uncertainties at this stage of design. The front and back webs are fastened to the top and bottom

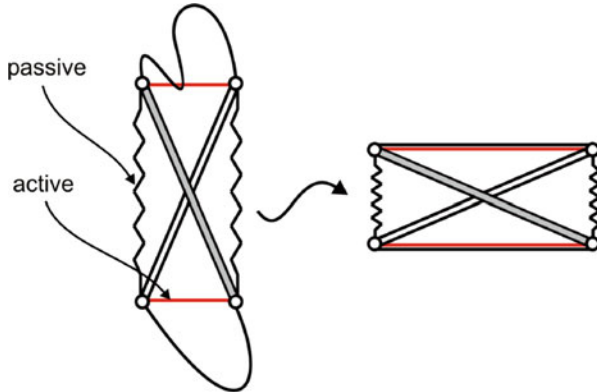


Fig. 24 A simple 2D structure exemplifying Deployment Phase 1. In an SR, the active and passive elements are, respectively, the hoop cables and the vertical cables. Polygonal cables have fixed length; they are slack before completion of Deployment Phase 1

polygons of the TR; moreover, they are linked to each other by means of tension elements, called tension ties. The reflecting mesh is fastened to the top web by means of tension elements distributed all over its surface, so as to give it the required working shape. The TR is composed of groups of cables identified as specified in Sect. 3.5 and shown in Fig. 25. Notice the additional group consisting of two continuous cables, henceforth referred to as the hoop cables, running in parallel to the top and bottom polygons, whose service function is explained below. Recall that some of the cables maintain a fixed length both in stowed and in deployed configuration (except of course for the modest lengthening due to tension), while the other cables change their length during deployment: precisely, vertical cables shorten, hoop cables lengthen. A vertical cable is shortened by pulling it inside a bar tube, by means of the deployment passive actuator described below; the cable portion remaining outside the bar after shortening is visible in Fig. 25.

The two hoop cables, the one running through the top-polygon nodes the other running through the bottom-polygon nodes, are lengthened by unwinding them from pulleys driven by electrical motors (the deployment active actuators) with controlled speed. Their function is to regulate the deployment speed during Deployment Phase 1: at the end of Deployment Phase 1, they become slack and have no structural role in the fully deployed configuration. On the contrary, polygonal cables are slack during Deployment Phase 1 and become in tension at the end of Deployment Phase 1 (see Fig. 24 for an illustration of such deployment strategy in a simple 2D example). They inherit the structural role of the hoop cables, starting from Phase 2 of deployment and, later, in the fully deployed configuration (polygonal and hoop cables appear overlapped in Fig. 25). Finally, diagonal and saddle cables are always in tension, both in the folded and deployed configurations and during deployment).

Deployment is implemented by the actuation systems mentioned above. There are 24 passive deployment actuators (one inside each tubular bar), which pull

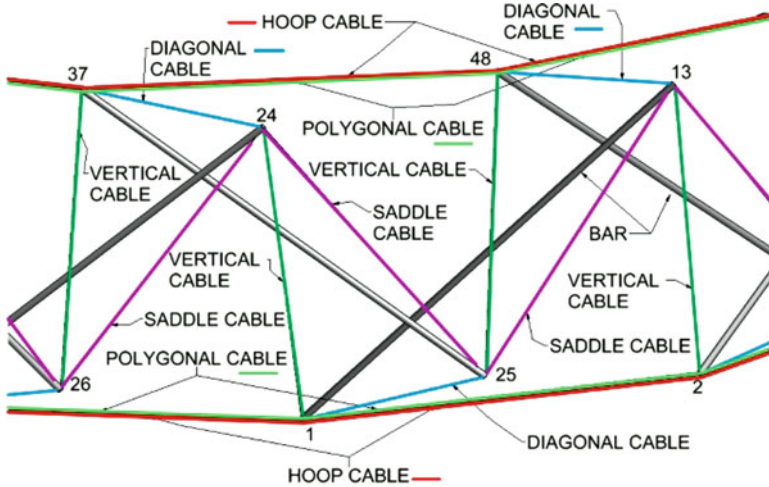


Fig. 25 TSS cables nomenclature (*close-up view of a portion of the TSS*)

vertical cables inside the tubes; by means of pre-loaded springs, they provide the force needed during Phase 1. Each of the two active deployment actuators consists of a rotating electrical motor and a pulley, where a hoop cable is coiled in the folded configuration they unwind the hoop cables, making sure that deployment proceeds in a smooth way by controlling the deployment speed (in their absence, Phase 1 would last only a few seconds, due to the action of the pre-loaded springs, and this could cause uncontrolled perturbations not only of the TSS but also of the spacecraft). Phase 1 ends when passive actuators have come to the end of their strokes, locking devices have reached the locked position, and hoop cables are completely unwound (the locking devices fix the position inside the bars of the endpoints of vertical cables, henceforth keeping their length fixed). At the end of Phase 1, the TSS has shape and dimensions close to the final ones; however, its stiffness is still low, because the cables do not have the design tension yet: specific actuators take care of this, during Phase 2. The three tensioning actuators are mounted 120° apart in the top polygon, so as to apply the required tension to three of the diagonal cables, and hence to all the dependent cables. Tensioning actuators apply tension by reducing the distance between the points to which the diagonal cables are fastened. As a consequence, during Deployment Phase 2 the TSS geometry is slightly modified.

The TSS Flight Model is attached to the spacecraft boom by means of an interface structure denoted by I/F, consisting of a plate (where the boom is attached) and three arms connected to three nodes of the TSS. Three cylindrical hinges and three spherical hinges are used to connect the arms to the plate and to the TSS (see the sketch in Fig. 26). The two active deployment actuators that unwind the hoop cables during Phase 1 are also mounted on the I/F.

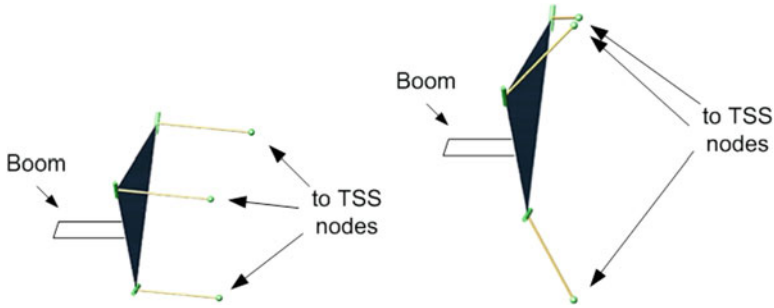


Fig. 26 TSS-to-Boom I/F. *Left*: deployed configuration; *right* folded configuration

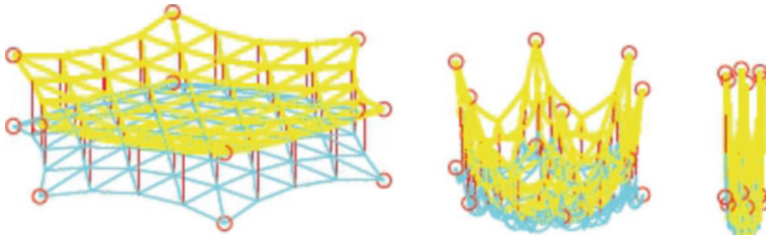


Fig. 27 Simulation of the RF mesh supporting web configuration (*red lines* represent the tension ties). *Left*: fully deployed ($D = 12$ m). *Center*: partially folded ($D = 6$ m). *Right*: fully folded ($D = 0.6$ m)

An important role in the TSS functions is assigned to the reflective mesh and to the web. The material of choice for the radio-frequency (RF) reflective surface must have low density and be easily foldable into a compact shape. The most common surface material for space reflectors of moderate precision is a mesh knitted from metallic or synthetic fibers plated with RF reflective material. The mesh must be sufficiently compliant to match without wrinkling the web's double-curvature surface. As the most recent studies suggest [8], 5 N/m is a mesh-tension value sufficient for operating frequencies up to 14 GHz. Since earlier studies also find this value suitable, we selected it as the nominal tension in the reflective mesh of our antenna. The relevant web configuration was analyzed (for the dimensions of triangle sides and web tension, see Fig. 27).

The tension-truss concept requires that the triangulated web is put under tension by loads approximately perpendicular to the surface of the antenna. The tension-truss concept is used in several antennas, currently operating in orbit. Its main advantage is that the geometric accuracy of the paraboloidal surface can be increased without any need to change the configuration of the supporting ring structure. The configuration of tension ties for the TSS was analyzed (e.g., axial/non-axial tension ties), and deployment simulations were performed. Our analyses suggested to avoid non-axial tension ties. To conform to the no-elongation and easy-tensioning requirements, a tension-tie configuration was identified and studied for a five-ring

web assembly. This solution, which is in our opinion the simplest one, can be adopted also for a larger number of rings.

Mesh folding and stowage is critical and should be studied in detail, as for state-of-the-art large reflectors. Mesh development activities include tests to characterize mesh mechanical properties including tendency to self-adhesion. The absence of external mechanical joints is considered advantageous also in relation to reducing the risk of mesh entanglement. The launch regime will be addressed by designing a suitable hold-down and release system for the deployable boom plus reflector dish assembly. There will be primary hold-down mechanisms to hold-down the deployable boom to the spacecraft lateral panel, and secondary hold-down mechanisms to restrain the reflector dish in its folded state and release it when boom deployment is completed.

In Europe, ESA [9] has already pre-qualified a deployable boom system with associated motorized deployment mechanisms and hold-down release system for a large reflector antenna of 12 m aperture. The problem of designing the mechanical connection between the reflector dish and the deployable boom has been addressed and included in the present development.

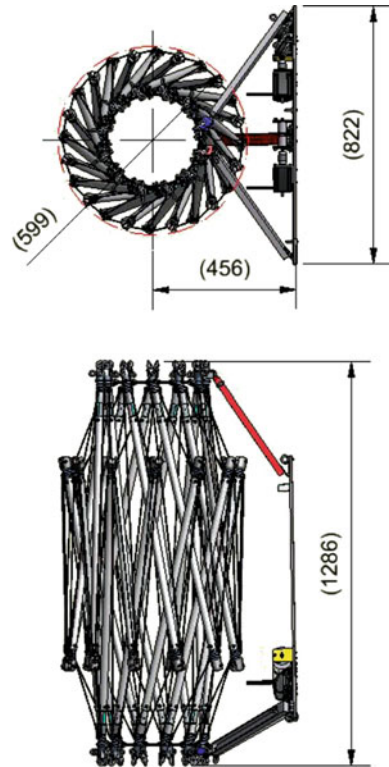
4.3 Breadboard Design

We performed a detailed design of a breadboard (BB) having all of the main structural features of the Flight Model described above. The TSS BB consists of the following main components: cables, bars, a simplified web consisting of radial cables, deployment actuation system, tensioning actuation system, and TSS-to-Boom I/F (Figs. 28 and 29). The BB is a scaled version of the TSS flight concept, designed according to the following rules:

- the polygon has the same number of sides (12) as the flight concept;
- the scaling ratio 1-to-4 applies to the overall deployed dimensions;
- the dimensions of the components (e.g., joints, cable, and bar cross-sections) may not be equally scaled.

The rigid parts of the BB were made mainly of aluminum and stainless steel; for cables, VectranTM was used; cable terminals were realized with the use of thimbles and ferrules. Bars are composed of a tube and two joints, one for each bar end. The two joints of a bar are obtained by assembling machined parts, and include the interfaces between that bar and all the relative cables. Each bar includes, inside the tube, a passive deployment actuator, used to shorten a vertical cable. Such an actuator pulls inside the bar a portion of the cable, shortening the cable portion external to the bar. During deployment, the cable is retracted into the bar, so that the distance between the two bars connected by that cable is reduced (for this reason, such a cable is also referred to as a shortening cable). The 24 passive actuators inside the bars provide, by means of compression springs, the force needed to deploy the structure in the course of Phase 1. Each passive actuator includes a locking

Fig. 28 TSS BB folded dimensions, in mm (the web is not shown in this figure)



device, which is needed to lock the shortening cable (vertical cable) into position and to fix its length, after Phase 1 is completed. The two joints located at a bar's ends are different, because the cables they join have different roles, and also because there is a cable that enters the bar tube at only one of its ends and is pulled by the passive actuator during deployment. The two joints are called joint A and joint B, with the cable being retracted into joint B.

The BB web consists of two sets of radial cables, joining the top-polygon vertices with the top-polygon center point and the bottom-polygon vertices with the bottom-polygon center point. Two discs collect, respectively, the top radial and the bottom radial cables; they are connected by an elastic member called the tension tie (see Fig. 30).

The BB was provided with a gravity compensation system (GCS), to reduce as much as possible gravity effects during deployment. The GCS is composed of an aluminum plate, called GCS plate, fixed to the ceiling of the laboratory, and of the cables by which the BB is attached to the GCS plate. 12 out of 24 of the BB bars are attached to the GCS plate. The three tensioning actuators and the TSS-to-Boom I/F are also attached to the GCS plate. The TSS-to-Boom I/F is attached to the GCS plate by means of three cables. GCS cables are composed of series of springs and a rope cable (of the same material used for the BB cables). The

Fig. 29 TSS BB deployed dimensions, in mm (the web is not shown in this figure)

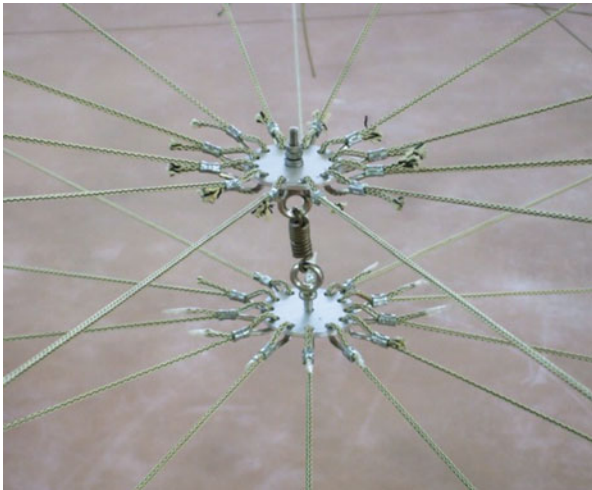
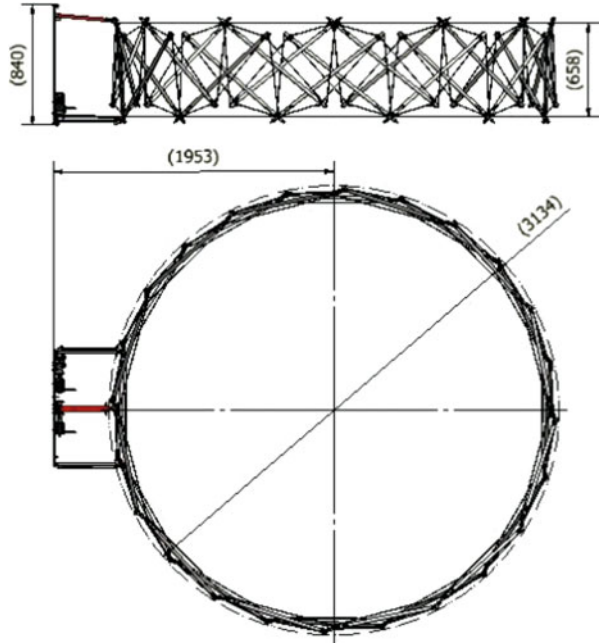
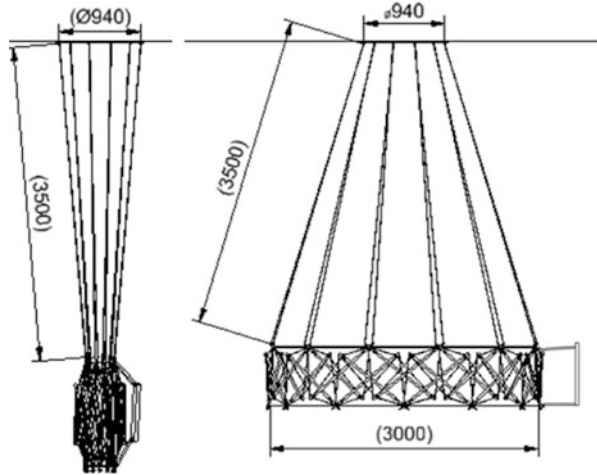


Fig. 30 TSS BB Web. The single tension tie includes a spring

Fig. 31 TSS BB attached to the GCS. *Left: folded, right: deployed*



number and the elastic properties of the springs are selected so as to decouple the natural frequency due to GCS cables from the natural frequency of the TSS ring (in particular, the springs that equip the suspension cables provide a natural frequency of about 0.5 Hz in the vertical direction). Figure 31 shows the BB attached to the GCS; the relevant reference dimensions are indicated; it is also shown how the TSS-to-Boom I/F modifies its shape on unfolding. In the unfolded configuration, the horizontal component of the GCS constraining force applied to the BB ring is about 20 % (peak value) of the vertical one. A moving mass is used to compensate the radial component of the TSS-to-Boom I/F weight force.

5 Breadboard Test Campaign

A test campaign was performed on the breadboard described above, including:

1. BB Geometry and Shape Test;
2. BB Performance Test (deployment and folding-up);
3. BB Structural Test (stiffness);
4. BB Stop-and-Go Test.

Figures 32 and 33 show the TSS BB attached to the GCS cables; the TSS-to-Boom I/F is visible on the left.

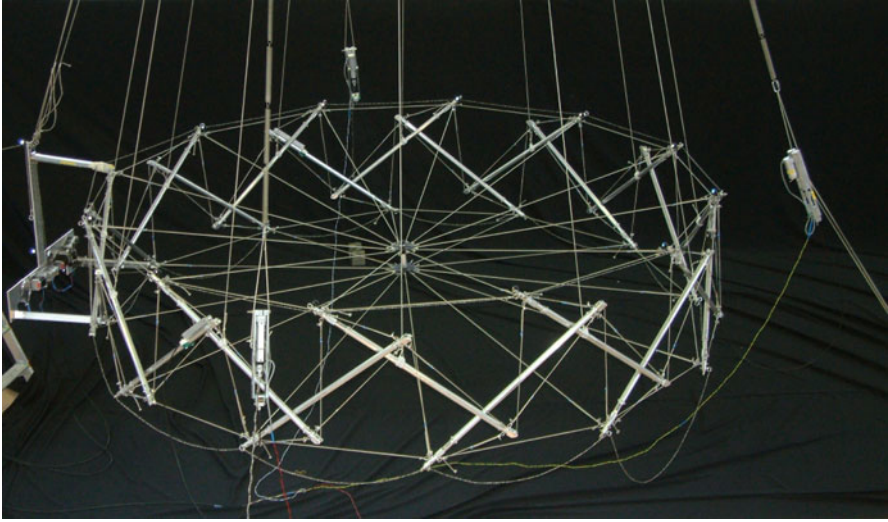


Fig. 32 TSS BB attached to the GCS. Deployed configuration—*top-side view*

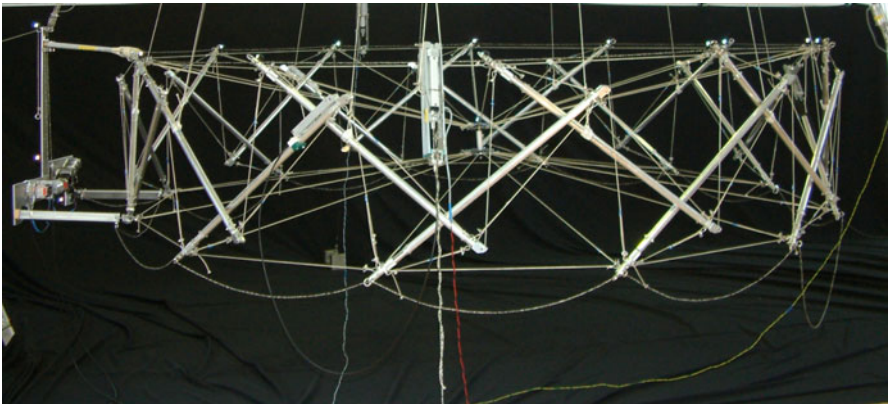


Fig. 33 TSS BB attached to the GCS. Deployed configuration—*side view*

5.1 BB Geometry and Shape Test

This test was aimed at measuring the geometrical-shape repeatability of the structure in the deployed configuration. The position of some points of the deployed structure after different stowing/deployment sequences was measured and the relevant differences in position between one stowing/deployment sequence and the others were calculated (post-processing). Three folding/deployment sequences were performed and the geometry data acquired (three repetitions). A total station

(laser measurement) was used to acquire the position of 15 markers placed on the BB. The data were elaborated in two ways:

- Calculating the distances of all the marker pairs and the relevant statistics (mean and standard deviation). The calculated mean of the standard deviation for markers located on the top polygon's sides was 0.34 mm.
- Calculating by orthogonal regression the fitting planes for markers placed on the TR top polygon's nodes. For the point distances from the fitting plane calculated for the three acquisitions, this elaboration showed a variance between 0.03 and 0.36 mm and a standard deviation between 0.16 and 0.6 mm.

All in all, the test showed a good repeatability of the folding/deployment process.

5.2 Breadboard Performance Test

The aim of this test was to verify that the deployment of the structure worked smoothly, with no bar and/or cable entanglements. Five folding/deployment complete sequences were performed. One entanglement only occurred, during sequence no. 4, due to the wrong folding of one of the cables that prevented complete deployment.

5.3 Breadboard Structural Test and analysis

The aim of this test was to measure the natural frequencies of the BB. Two tri-axial accelerometers were placed on the structure and the response to in-plane and out-of-plane perturbations of the ring was recorded. The in-plane perturbation was introduced by means of a rope passing through diametrically opposite bars ends of the top and bottom polygons. The rope length was such as to reduce the diametral distance of the connected bar ends (i.e., ring forced to an elliptical shape). The rope was then cut causing the perturbation in the radial direction. The out-of-plane perturbation was introduced by constraining a bar end of the ring structure to the ground, so as to force the ring into a cantilever-like bent shape. The rope was then cut, causing a bending-mode perturbation.

In addition to the 0.5 Hz design frequency of the GCS in vertical direction, the next eight measured frequencies were at 1.2, 2.7, 5.4, 7.8, 10.3, 11.1, 13, and 13.8 Hz. Figures 34 and 35 show the recorded power spectrum relevant to, respectively, in-plane perturbation and out-of-plane perturbation.

A structural analysis was performed before and after the test campaign. Besides the frequencies relevant for the GCS, the analysis indicated that two out-of-plane natural frequencies (at, respectively, 11.0 and 11.2 Hz) affected all nodes in a bending motion of the annular structure. Note that, as per visual inspection, the various types of modes are often coupled to each other, due to the fact that

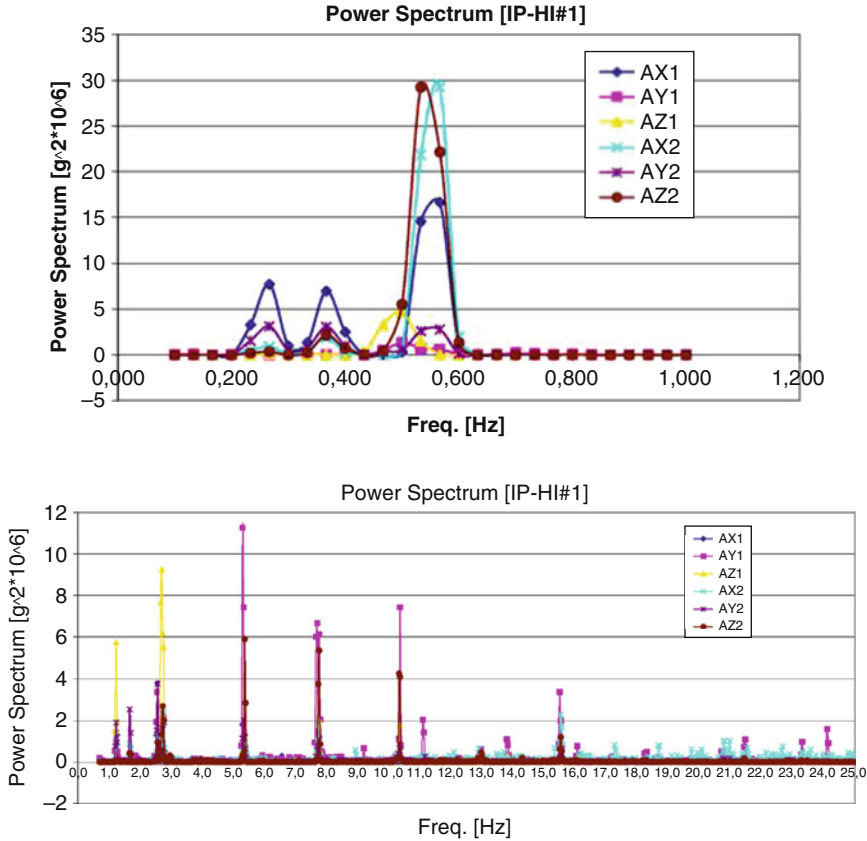


Fig. 34 TSS BB—recorded power spectrum vs. frequency. In-plane perturbation

frequencies are close to each other. This can be seen, for example, in Fig. 36 left, where the out-of-plane bending of the TSS is coupled with the transversal vibration of the GCS supporting the IF.

The in-plane modes involve intermediate nodes only, without affecting nodes at the vertices of the base polygons. In these modes, the motion of the intermediate nodes is directed radially in the horizontal plane. The 17 calculated frequencies are in the range between 6.7 and 14.1 Hz. The structural analysis also shows that the modes associated with the GCS correspond to the first peaks appearing in the power spectrum from the tests. The correspondence is quite clear for frequencies of about 0.5, 1.2, 2.7, and 5.4 Hz. The frequency of the first modes involving intermediate nodes (about 7, 8 and 10 Hz) are located in proximity of the peaks of the spectrum obtained from the tests. A correspondence between the frequency of the first out-of-plane bending mode at 11 Hz and relevant peak in the spectrum is also visible.

The results of the analysis are in a fairly good agreement with those of the test, even though the dynamic response of the BB can, in principle, be coupled with

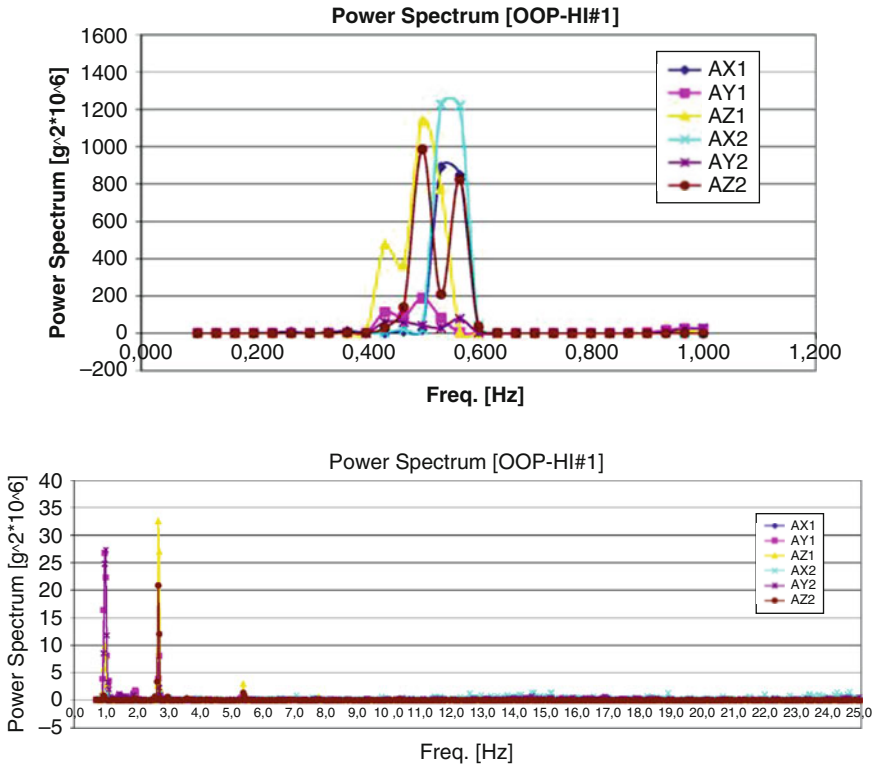


Fig. 35 TSS BB—recorded power spectrum vs. frequency. Out-of-plane perturbation

that of the GCS. A modal analysis in the absence of gravity was performed for both the BB and the FM. In both cases, the first mode is an out-of-plane cantilever-like bending mode, with frequency of 1.9 Hz for the BB and 2.1 Hz for the FM. In consideration of the fairly good agreement between tests and numerical simulations, these results show that the FM should have good dynamic performance, since its first natural frequency is not only higher than 1 Hz but also indeed far away from this value.

5.4 Breadboard Stop-and-Go Test

This test was aimed to demonstrate the capability of the TSS BB to complete deployment even if a stop occurs during deployment. The deployment was started and stopped after 30 s, before Phase 1 was completed (in nominal conditions, Phase 1 is completed in 2 min). After a 60 s stop, deployment was re-started until a successful completion, including Phase 2.

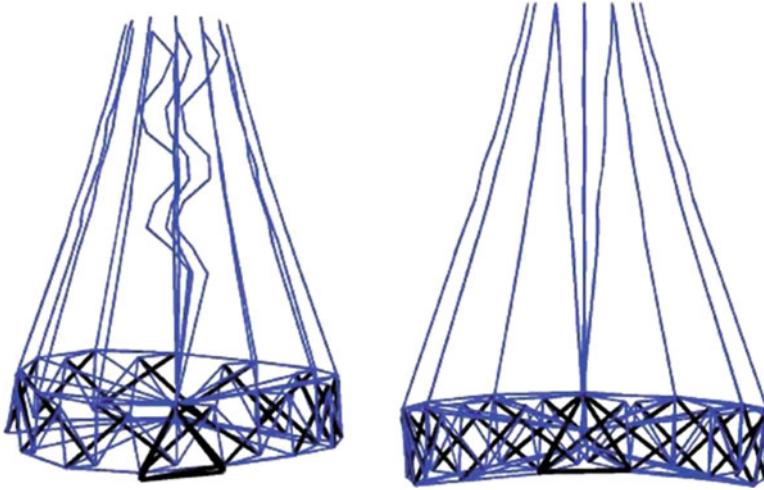


Fig. 36 *Left:* out-of-plane bending, coupled with transversal vibrations of the GCS, 11.0 Hz. *Right:* Out-of-plane bending, 11.2 Hz

6 Conclusions

The successful development of a new architectural concept of a large deployable reflector (about 12 m in diameter) for space applications has been achieved and presented in this paper. By exploiting “tensegrity” structural principles, a large deployable ring has been conceived, which does not include any mechanical joint or articulation between its rigid members, which are interconnected only by cables. Having no mechanical joints in the expandable ring, therefore eliminating a major potential source of single-point failures, constitutes a major advantage in terms of deployment reliability, a crucial requirement for such systems. The new architecture has been studied in detail, and a reduced-scale breadboard model (3 m in diameter) has been realized and tested to validate the main design features. Means to interface the expandable ring to the hosting spacecraft have been studied in detail, resulting in an innovative and very efficient solution. A suitable gravity off-loading system has been designed and implemented for the test campaign of the reflector breadboard. All major design assumptions and features have been validated during the test campaign, namely: deployment functionality (including “Stop-and-Go” deployment verification); deployment accuracy/repeatability; and stiffness in deployed configuration. The newly conceived architecture, which has been protected by an international patent filing, is a potential candidate for further development studies to reach higher technology readiness level (TRL) as well as, possibly, for an in-orbit deployment demonstration. ESA has established a roadmap to increase large deployment reflector TRL status [9] and a research and development activity has recently started for the development of a suitable RF mesh.

References

1. Burkhardt, B.: Synergetics gallery. <http://bobwb.tripod.com/synergetics/photos/index.html>. Cited Feb 2016
2. Datashvili, L., Maghaldadze, N., Endler, S.: Advances in mechanical architectures of large precision space apertures. In: Proceedings of the 13th European Conference on Spacecraft Structures, Materials & Environmental Testing, 1–4 Apr 2014, Braunschweig
3. ESA webpage on future missions http://www.esa.int/Our_Activities/Observing_the_Earth/The_Living_Planet_Programme/Earth_Explorers/Future_missions/About_future_missions. Cited March 2016
4. Gómez Jáuregui V.: Controversial origins of tensegrity. In: Domingo, A., Lazaro, C. (eds.) Proceedings of the IASS Symposium 2009, Valencia (2009)
5. Harris Corporation: Unfurlable Antenna Solutions. http://govcomm.harris.com/solutions/space_systems/unfurlablemeshantennareflectors.aspx. Cited Feb 2016
6. Hernandez, S.J., Mirats Tur, J.M.: Tensegrity frameworks: Static analysis review. *Mech. Mach. Theor.* **43**, 859–881 (2008)
7. Li, B., Luo, A., Liu, R., Tao, J., Liu, H., Wang, L.: Configuration modeling and interior force analysis of deployable tensegrity. In: Proceedings of the 14th IFToMM World Congress, Taipei, 2015, pp. 126–131 (2015)
8. Lubrano, V., Mizzoni, R., Silvestrucci, F., Raboso, D.: PIM characteristics of the large deployable reflector antenna mesh. In: 4th International Workshop on Multipactor, Corona and Passive Intermodulation in Space RF Hardware, Noordwijk (2003)
9. Mangenot, C., Santiago-Prowald, J., van't Klooster, K., Fonseca, N., Scolamiero, L., et al.: Large Reflector Antenna Working Group, Executive Report, TEC-EEA/2010.636/CM, ESA, Estec, Noordwijk (2010)
10. Micheletti, A.: The indeterminacy condition for tensegrity towers, a kinematic approach. *Revue Française de Génie Civil* **7**, 329–342 (2003)
11. Micheletti, A.: Bistable regimes in an elastic tensegrity systems. *Proc. R. Soc. A* **469**, 20130052 (2013)
12. Micheletti, A., Williams, W.O.: A marching procedure for form-finding for tensegrity structures. *J. Mech. Mater. Struct.* **2**, 857–882 (2007)
13. Northrop-Grumman: Astromesh^l. http://www.northropgrumman.com/businessventures/astro_aerospace/products/pages/astromesh.aspx. Cited Feb 2016
14. Oppenheim, I.J., Williams, W.O.: Tensegrity prisms as adaptive structure. In: Adaptive Structures and Material Systems, vol. 54, pp. 113–120. ASME, Dallas, TX (1997)
15. Peng, Z., Yuan, X., Dong, S.: Tensegrity torus. In: Proceedings of the IASS-ACPS 2006, Beijing (2006)
16. Scialino, G.L., Salvini, P., Migliorelli, M., Pennestrì, E., Valentini, P.P., van't Klooster, K., Santiago Prowald, J., Rodrigues, G., Gloy Y.: Structural characterization and modelling of metallic mesh material for large deployable reflectors. In: Proceedings of the Advanced Lightweight Structures and Reflector Antennas, 1–3 Oct 2014, Tbilisi, GA (2014)
17. Scolamiero, L., Zolesi, V.S., Ganga, P.L., Podio-Guidugli, P., Micheletti, A., Tibert, A.G., in the name of European Space Agency, International Patent for “A Deployable Tensegrity Structure, Especially For Space Applications”, Patent Application: PCT/IB2012/051309, filed Mar 2012
18. Snelson, K.D.: personal webpage <http://www.kennethsnelson.net>. Cited Feb 2016
19. Stern, I.: US Patent for a “Deployable reflector antenna with tensegrity support and associated method”, No. 6,542,132, Apr 1, 2003
20. Thomson, M.W., Marks, G.W., Hedgepeth, J.M.: US Patent for a “Light-weight reflector for concentrating radiation”, No. 5,680,145, Oct 21, 1997
21. Tibert A.G., Pellegrino, S.: Review of form-finding methods for tensegrity structures. *Int. J. Space Struct.* **18**, 209–223 (2003)

22. Yuan, X., Peng, Z., Dong, S., Zhao, B.: A new tensegrity module - 'torus'. *Adv. Struct. Eng.* **11**, 243–252 (2008)
23. Zolesi, V., Ganga, P., Scolamiero, L., Micheletti, A., Podio-Guidugli, P., Tibert, A.G., Donati, A., Ghiozzi, M.: On an innovative deployment concept for large space structures. *Proceedings of 42nd International Conference on Environmental Systems (ICES)*, AIAA 2012-3601, San Diego, CA, 15–19 July 2012